Biomedicine & Pharmacotherapy 183 (2025) 117815

Contents lists available at ScienceDirect

Biomedicine & Pharmacotherapy

journal homepage: www.elsevier.com/locate/biopha

HEBE: A novel chimeric chronokine for ameliorating memory deficits in Alzheimer's disease

Jon Esandi [a,b], Pedro Renault [c,d,e], Maria Dolores Capilla-López [a,f], Rebeca Blanch [a,b], Ángel Edo [a,b], David Ramirez-Gómez [a,b], Assumpció Bosch [a,b], Beatriz Almolda [a], Carlos Alberto Saura [a,f], Jesús Giraldo [c,d,e], Miguel Chillón [a,b,g,*]

[a] Institut de Neurociències (INc), Universitat Autònoma Barcelona, Bellaterra 08193, Spain
[b] Vall d'Hebron Institut de Recerca (VHIR), Barcelona 08035, Spain
[c] Laboratory of Molecular Neuropharmacology and Bioinformatics, Unitat de Bioestadística, Universitat Autònoma de Barcelona, Bellaterra 08193, Spain
[d] Unitat de Neurociència Translacional, Parc Taulí Hospital Universitari, Institut d'Investigació i Innovació Parc Taulí, Universitat Autònoma de Barcelona, Bellaterra 08193, Spain
[e] Centro de Investigación Biomédica en Red de Salud Mental (CIBERSAM), Instituto de Salud Carlos III, Bellaterra 08193, Spain
[f] Centro de Investigación Biomédica en Red Sobre Enfermedades Neurodegenerativas (CIBERNED), Instituto de Salud Carlos III, Madrid 28029, Spain
[g] Institució Catalana de Recerca i Estudis Avançats (ICREA), Barcelona 08010, Spain

ARTICLE INFO

Keywords:
Alzheimer's disease
Chronokine
Chimeric protein
HEBE
Klotho
TREM2
TIMP2
Memory impairment

ABSTRACT

Alzheimer's disease (AD) is a prevalent neurodegenerative disorder characterized by amyloid-β and Tau protein depositions, with treatments focusing on single proteins have shown limited success due to the complexity of pathways involved. This study explored the potential of chronokines —proteins that modulate aging-related processes— as an alternative therapeutic approach. Specifically, we focused on a novel pleiotropic chimeric protein named HEBE, combining s-KL, sTREM2 and TIMP2, guided by bioinformatic analyses to ensure the preservation of each protein's conformation, crucial for their functions. *In vitro* studies confirmed HEBE's stability and enzymatic activities, even suggesting it has different activities compared to the individual chronokines. *In vivo* experiments on APP/Tau mice revealed improved learning and memory functions with HEBE treatment, along with decreased levels of phosphorylated Tau and minor effects on amyloid-β levels. These findings suggest that HEBE is as a promising therapeutic candidate for ameliorating memory deficits and reducing pTau in an AD mouse model.

1. Introduction

Alzheimer's disease (AD) stands as the predominant form of dementia worldwide, encompassing 60–80 % of all cases [1]. The histopathological underpinnings of this neurodegenerative disorder are marked by the accumulation of aggregated amyloid-β (Aβ) and Tau species [2], along with neuroinflammatory processes [3]. These pathological alterations result in synaptic depletion, neuronal death, and cognitive decline in affected individuals [4]. Despite extensive research, the underlying causes of AD remain poorly understood, hindering the development of effective therapeutic interventions. In this context, chronokines -proteins with pleiotropic effects that influence aging and systemic homeostasis- have emerged as a potential therapeutic innovation[5]. Although chronokines such as sKL exhibit pleiotropic effects [6,7], they might not be sufficient as a standalone therapy for AD. Therefore, leveraging the technology of chimeric proteins, we proposed a strategy combining different chronokines with complementary functions to enhance their therapeutic efficacy.

Chimeric proteins are being widely studied for several applications, as they offer advantages such as extended half-life and enhanced therapeutic effects, among others. Typically, FDA-approved chimeric proteins consist of a short effector peptide linked to a protein that helps with stability, targeting, and solubility, such as the Fc region of the human IgG1 antibody [8]. The effector peptide typically modulates the activity

* Correspondence to: Universitat Autònoma de Barcelona, Avenida de la Vall Moronta s/n, Edifici H 5ªplanta, Bellaterra, Barcelona 08193, Spain.
E-mail addresses: jon.esandi@uab.cat (J. Esandi), pedro.renault@uab.cat (P. Renault), lolacapilla03@gmail.com (M.D. Capilla-López), rebeca.blanch@uab.cat (R. Blanch), angel.edo93@yahoo.es (Á. Edo), david.ramirez@uab.cat (D. Ramirez-Gómez), assumpcio.bosch@uab.cat (A. Bosch), beatriz.almolda@uab.cat (B. Almolda), carlos.saura@uab.cat (C.A. Saura), jesus.giraldo@uab.cat (J. Giraldo), miguel.chillon@uab.es (M. Chillón).

https://doi.org/10.1016/j.biopha.2025.117815
Received 9 August 2024; Received in revised form 5 January 2025; Accepted 9 January 2025
Available online 15 January 2025

of a specific receptor either as an agonist or antagonist. Additionally, another area where chimeric proteins find application is in cancer immunotherapy involving CAR T-Cells, where the CAR receptor of the T-Cells is engineered to bind to specific antigens on the surface of cancer cells [9]. In this study, we developed a new chimeric chronokine named HEBE, incorporating three distinct chronokines (s-KL, sTREM2, and TIMP2), each possessing established beneficial functions for AD.

The first chronokine, αKlotho, is a pleiotropic protein associated with anti-aging properties. Mutations in the *klotho* gene have been linked to accelerated aging phenotypes in murine models, manifesting in reduced lifespan, infertility, and arteriosclerosis, among other traits [10]. Mutant mice deficient in Klotho show clear signs of neurodegeneration, with impaired memory and increased oxidative stress [11], decreased levels of synaptic proteins [12] and deficient axonal transport [13]. The Klotho protein presents different isoforms, the full-length being a transmembrane protein called m-KL [14], and an alternative splicing variant leading to a secreted form of the protein called s-KL. In particular, the s-KL isoform has been shown to protect against age-dependent memory deficits [6,7].

The second chronokine, Triggering Receptor Expressed on Myeloid Cells 2 (TREM2), is a transmembrane protein predominantly expressed in microglial cells. Cleavage of TREM2 by ADAM10 and ADAM17 yields a soluble fragment termed sTREM2 [15]. This protein plays pivotal roles in microglial-mediated clearance of apoptotic neurons, damaged myelin, and amyloid plaques [16]. Furthermore, it modulates microglial biosynthetic pathways, cytokine production, and the recruitment of microglia to amyloid deposits [17]. Consequently, sTREM2 mitigates amyloid plaque accumulation and associated neurotoxicity [18]. Notably, mutations in the TREM2 gene predispose individuals to AD [19], while sustained expression of sTREM2 via adeno-associated virus (AAV) vectors has shown promise in reducing amyloid burden and ameliorating synaptic and cognitive deficits in murine AD models [17].

The third chronokine, Tissue Inhibitor of Matrix Metalloproteinases 2 (TIMP2), is a protein enriched in young mouse plasma that increases synaptic plasticity and hippocampus-dependent cognition when injected into aged mice [20,21], and is involved in promoting neuronal differentiation [22]. Additionally, TIMP2 plays crucial roles in maintaining tissue homeostasis by inhibiting quiescent tissue proliferation in response to angiogenic stimuli, independent of its matrix metalloproteinase (MMP) inhibitory functions [23]. Consequently, TIMP2 emerges as a promising candidate for ameliorating vascular dysfunction, a hallmark of AD pathology.

The resulting chimeric chronokine is named HEBE, from the Greek goddess of rejuvenation *Hebe*.

2. Materials and methods

2.1. Animals

This study was carried out in strict accordance with the current National regulations. The Committee on the Ethic of Animal Experiments of the Universitat Autònoma de Barcelona approved the procedures described (protocol number: CEEAH 4882). Mice were bred in Macrolon cages, fed ad libitum with standard diet, and kept under controlled temperature (22 ± 2 °C) and light-dark cycles (12 h). Littermate APP/Tau and control (WT) mice from APP and Tau transgenic crossing were used as models of AD[24]. Both male and female mice at 24 weeks of age were injected intravenously into the lateral tail vein of the mice with AAV9P31 vectors that expressed HEBE or Null as a control.

2.2. Cultured cell lines

The HEK-293 (ATCC #CRL-1573) cell line derived from a human embryonic kidney was used for plasmid transfection and protein expression. Cells were grown at 37 °C, 5 % CO_2 in DMEM (Lonza) containing 10 % Fetal Bovine Serum (Sigma) and 1X penicillin/streptomycin (Sigma). Plasmid constructs were transfected into HEK-293 using polyethylenimine (PolySciences).

The BV-2 (CLS #305156, Cytion) microglial cell line derived from C57BL/6 mice was used for the phagocytosis assay. Cells were grown at 37 °C, 5 % CO_2 in DMEM (Lonza) containing 10 % Fetal Bovine Serum (Sigma) and 1X penicillin/streptomycin (Sigma).

2.3. All-atom models

For Klotho, sTREM2 and TIMP2, all-atom models were built from the crystal structures in PDB entries 5W21, 5UD7 and 1BR9, respectively. The model for Klotho included residues E34-V534 of chain A of 5W21.pdb. A stretch of 18 residues (L98-S115) absent from the crystal was included using Modeller [25]. For sTREM2, all residues (T21-A157) of the chain F of 5UD7.pdb were retained. For TIMP2, all residues (C1-A182) in 1BR9.pdb were included (12 C-terminal residues not seen in the crystal structure were not added to the model).

2.4. All-atom MD simulations

For each protein, titratable residues were attributed their dominant protonation state at pH 7.4. Neutral groups were added to cap the N- and C-termini of each protein chain. The software HTMD [26] was employed to solvate and ionize the proteins. Each protein was inserted in a water box whose edges were at a minimum distance of 12 Å from the solute. Ions were added to neutralize charges and up to a concentration of 0.15 M NaCl.

After 500 steps of energy minimization with the conjugated gradient method, systems were equilibrated for 3 ns in the NPT ensemble, with temperature of 300 K and pressure of 1 atm. Harmonic position restraints of 1.0 kcal mol^{-1} $Å^{-2}$ were applied to the Cα atoms, while restraints of 0.1 kcal mol^{-1} $Å^{-2}$ were applied to the remaining heavy atoms of the protein. These restraints were progressively released during equilibration. Production simulations of 520 ns were performed in the NVT ensemble, at 300 K. In all stages, temperature was controlled by a Langevin thermostat, a 9.0 Å cut-off was used for non-bonded interactions, and long-range electrostatic interactions were calculated with the particle-mesh Ewald (PME) method. Hydrogen mass repartitioning allowed a timestep of 4 fs. The ff14SB [27] force field was used for proteins, and water was described by the TIP3P model [28]. We employed the Acemd 2 [29] software to run the trajectories.

2.5. Analysis of all-atom MD simulations

Principal Component Analysis (PCA) consisted in the diagonalization of the covariance matrix, whose elements are:

$$C_{ij} = \left\langle (r_i - \langle r_i \rangle) \bullet (r_j - \langle r_j \rangle) \right\rangle$$

where i and j denote all pairs of the 3 N Cartesian coordinates of the N Cα atoms in the protein. The vector r_i indicates the instantaneous value of coordinate i and $\langle r_i \rangle$ is the average value of this coordinate in the ensemble of conformations. The coordinates of the Cα atoms in each individual trajectory were projected on the space of the respective first two principal components. These analyses were performed with the Gromacs software [30].

Root-mean-square fluctuations (RMSF) were also calculated with Gromacs, according to the expression:

$$RMSF_i = \sqrt{\left\langle (r_i - \langle r_i \rangle)^2 \right\rangle}$$

where r_i denotes the coordinates of atom i.

Root-mean-square deviations (RMSD) were also calculated with Gromacs, according to the expression:

$$\mathrm{RMSD} = \sqrt{\frac{1}{N}\sum_{i=1}^{N}\left(r_i - r_i^{ref}\right)^2}$$

Where r_i is the set of coordinates of an atom, and r_i^{ref} represents the set of coordinates of the i atom in the reference structure.

2.6. Construction of models of the united proteins

These models were built by homology modeling using Modeller [25]. A single sequence, consisting of the sequences of the three proteins and the linkers arranged in the desired order, was defined as the target, and the structures of Klotho, sTREM2 and TIMP2 were used as templates. Additional restrictions were added to enforce the helical secondary structure of the linkers.

2.7. Coarse-grained MD simulations

The all-atom models of the united proteins were converted to coarse-grained (CG) representation using the "Martini Maker" functionality of the Charmm-gui webserver[31]. The systems were described by the Martini 2.2 force field [32], with the addition of an elastic network composed of harmonic springs between interacting sites (elnedyn) to preserve the secondary and overall tertiary structures of each protein [33]. However, it is important to note that there were no inter-protein springs, so the relative motions of the three components were not restrained. The CG models were solvated and ionized up to a 0.15 M NaCl concentration. Each system was submitted to two independent simulation replicas. In each replica, after energy minimization with the steepest descent algorithm, equilibration in the NPT ensemble, with progressive release of position restraints on the protein, was run for 20 ns. Equilibration was followed by a 10 μs production in the NPT ensemble, with temperature of 300 K and pressure of 1 atm. Temperature was controlled with the v-rescale thermostat, and pressure was controlled with the Berendsen (during equilibration) and Parrinello-Rahman (during production) barostats. A dielectric constant of 15 was adopted, and electrostatic interactions as well as van der Waals interactions were shifted to zero between 0 and 11 Å. In equilibration and production, the timestep was 20 fs. All CG simulations were performed with the Gromacs software (version 2019) [30].

Trajectories were visually inspected for an assessment on protein aggregation.

2.8. Plasmid transfection in HEK-293 cells

Transfections were carried out in 6-well plates, using 3 μg of plasmid dissolved in 200 μL of 0.9 % NaCl (B.Braun). In a separate tube, 2.25 μL of polyethylenimine (PolySciences) per μg of DNA was diluted in 200 μL of NaCl. The DNA dilution was slowly mixed with the PEI solution, and left at RT for 20 min to form the DNA/PEI complexes. Then, the growth medium from each plate well was discarded and 500 μL of transfection medium was added (DMEM containing 1 % Fetal Bovine Serum), along with 240 μL of the DNA/PEI mixture. Plates were incubated at 37 °C and 5 % CO_2 for 3 h, and then the medium was discarded, and 3 mL of fresh growth medium was added.

2.9. Western Blot

Western blotting was performed on lysates from cell cultures and cell media. Samples were lysed in RIPA (50 mM Tris HCl, 150 mM NaCl, 1 % (v/v) NP-40, 0.5 % (w/v) Sodium Deoxycholate, 1 mM EDTA, 0.1 % (w/v) SDS, 0.01 % (w/v) sodium azide, pH 7.4) centrifuged at 10,000*g* for 10 min at 4 °C to remove the insoluble fraction. Protein concentration in lysates was determined using the BCA protein assay kit (Pierce).30 μg of lysates and cellular media were resolved on a 10 % Tris-glycine polyacrylamide gel at constant voltage, and then transferred to a PVDF membrane. After blocking with 5 % BSA in TBST for 1 h, membranes were incubated with the following primary antibodies in blocking buffer overnight at 4 °C: TREM2 (R and D Systems, 1:1000), TIMP2 (R and D Systems, 1:1000), Klotho (Sigma-Aldrich, 1:1000). Membranes were then incubated with HRP-conjugated antibodies (1:10,000) in blocking buffer for 1 h at room temperature. Membranes were washed and developed using the Westar EtaC Ultra 2.0 Western-Blot kit (Cynagen). Signal was acquired using Chemidoc MP (BioRad).

2.10. β-glucuronidase assay

10 μg of s-KL and equimolar amounts of the other indicated proteins diluted in 0.1 M citrate buffer were incubated with 0.5 mM of substrate 4-methylumbelliferyl β-D-glucuronide hydrate (Sigma M9130). The reaction was allowed to occur for 2 hours at 37 °C, and the fluorescence of the reaction product was measured with an excitation wavelength of 360 nm and an emission wavelength of 470 nM in a Spark plate reader (Tecan) following manufacturer's instructions. Bovine β-glucuronidase (Sigma G0251) served as a positive control, while PBS was used as a negative control.

2.11. MMP1 inhibition activity assay

In a 96-well plate, 1.6 μg/mL of MMP1 (PeproTech 420–01) was incubated with 30 μM substrate (Sigma SCP0193), 1 μg/mL of TIMP2, and equimolar concentrations of the other indicated proteins. The mixture was incubated for 30 minutes at room temperature and fluorescence was measured with an excitation wavelength of 324 nm and an emission wavelength of 400 nm in a Spark plate reader following manufacturer's instructions. The activity of TIMP2 was measured as the reduction in fluorescence due to the inhibition of MMP1 enzymatic activity on the substrate that yielded the fluorescent product. In the positive control, TIMP2 was omitted, and in the negative control MMP1 was not added.

2.12. Phagocytosis assay

BV2 cells (CLS) were seeded in 96-well plates. After 16 h of incubation with 2 μg/mL of sTREM2 and equimolar concentrations of the other indicated proteins, cells were exposed to 3 μM of FITC-Aβ_{1-42} (Bachem 4095738) or 15 μg/mL of myelin-pHrodo (Sigma M1891 and ThermoFisher P35369) for 3 h. Following trypsinization of the cells and an incubation with a PerCP Rat Anti-Mouse CD45 antibody (BD Biosciences, 1:500) for 30 min at 4 °C to label activated microglial cells, phagocytic activity was measured as the increase in intracellular fluorescence by flow cytometry in a CytoFLEX cytometer following manufacturer's instructions.

2.13. Viral vectors

Adeno-associated viral vectors AAV9P31 [34] carrying the HEBE or Null constructs were generated at the Unitat de Producció de Vectors (UPV) (www.viralvector.eu) following the triple transfection method [35]. Animals were simultaneously injected intravenously into the lateral tail vein of the mice, with $5{\cdot}10^{11}$ vg in 200 μL of 0.9 % NaCl.

2.14. Quantification of viral genomes

After DNase treatment (Thermo Scientific) and reverse transcription of RNA (Bioline) from liver and brain, a qPCR was performed with primers specific for the HEBE viral vector genome, and CycB as a housekeeping. 50 ng of cDNA was used, with 5 μL of iTaq Universal SYBR Green Supermix (BioRad), 0.3 mM of each oligonucleotide and MiliQ water to a final volume of 10 μL. A Hard-Shell Whin-Wall 384-Well Skirted PCR plate (BioRad) was filled with samples and sealed with Microseal Adhesive Seal (BioRad). Each sample was analyzed in

triplicates using the specific oligonucleotide pair for each gene (Thermo Fisher Scientific). HEBE-Fw: AATGGCTTCCCTCCTTTACC, HEBE-Rv: CTCGAAGCATTAACCCTCACT, Gapdh-Fw: AGGTCGGTGTGAACGGATTTG, Gapdh-Rv: TGTAGACCATGTAGTTGAGGTC, CycB-Fw: TCAACCTCTCCTCTCCTGCC, CycB-Rv: GGTTTCTCCACTTCGATCTTGC. The program used in the CFX384 Thermocycler (BioRad) was the same in all cases: 2 min at 98 °C for polymerase activation and cDNA denaturation, followed by 40 cycles of 5 s at 95 °C for denaturation and 30 s at 58 °C for annealing and extension. A calibration curve with known CycB amounts was used to extrapolate the CycB Cq, and normalize the HEBE Cq numbers per cell.

2.15. Open field

Mice were placed on a square wall-enclosed 40 × 40 cm white box, and were allowed to freely explore for 5 minutes. A digital camera was used to record the test, and was later analyzed with the Any-Maze software.

2.16. Novel object recognition test

The test consisted of 3 days. The Open Field test was used as the habituation day. On the familiarization day, 2 identical objects were placed inside the box, and the mouse had 10 minutes to explore them, expecting it to explore each object for the same amount of time. On the memory test day, one of the objects was replaced with a new one, and the mouse had 10 minutes to explore both objects. A digital camera was used to record the test, and the time that the mouse spent exploring each object was analyzed as the preference index with the Any-Maze software, where a longer time exploring the new object was indicative of better memory. The total exploration time in the familiarization and memory tests was used as an inclusion criterion, and only mice that spent more than 5 s exploring objects were included in the analysis.

2.17. Morris water maze

A 120 cm in diameter pool with opaque water was used for the test. The first day of the test (Cued test) consisted of the visual perceptual learning, where mice performed 4 trials of a maximum of 60 s to locate the platform that was visible over the water surface, with a small flag as a visual clue. Spatial learning was examined for the following 4 days, in which mice were trained (4 trials/day of a maximum of 60 s) to reach the platform that was 1.5 cm below the surface with the help of 4 visual clues around the pool. If a mouse failed to reach the platform, it was manually placed on it for 10 s. The platform remained in the same position throughout all the learning days, and mice entered the pool from different spots in each trial to encourage learning through the visual clues. The Any-Maze software was used to analyze the results.

2.18. Immunofluorescence

Brains embedded in OCT were cut into 12 μm slices. Samples for Aβ immunofluorescence underwent antigen retrieval through an incubation of 30 min in citrate buffer at 55 °C, followed by 30 min at RT in an 80 % formic acid solution. Samples were then permeabilized with cold methanol for 10 s for Aβ immunofluorescence, or 30 min in PBS-Tween 0.3 % for pTau. Samples were blocked for 1 h at RT with blocking solution (1 % BSA in PBST). Primary antibodies were then used for an overnight incubation at 4 °C, with anti-β-amyloid (BioLegend 803001, 1:200) or anti-phospho-Tau (pSer202/Thr205) (ThermoScientific MN1020, 1:200). Samples were then incubated with the Goat anti-mouse biotin secondary antibody (1:200) and Streptavidin-alexa 488 (1:500). Following 3 washes, samples were incubated for 10 min with Hoechst (1:500) to label the cell nuclei. Finally, samples were mounted with Fluoromount, and pictures were taken with the Eclipse 90i (Nikon) fluorescence microscope. Two slices per mouse were analyzed, and pTau and Aβ positive area was quantified using Fiji.

2.19. Statistical analysis

Data was analyzed by an investigator blind to the genotype or sex of mice. Results are expressed as the mean of the obtained values ± standard error of the mean (SEM). Statistical analyses were performed using the GraphPad software (version 9.0.1), with a parametric analysis, which was also used for the generation of graphs. Differences among more than two groups were evaluated using either One-way ANOVA (for one variable) or Two-way ANOVA (for two variables), followed by Tukey's post-hoc test. Differences between two means among test days in the MWM were evaluated using a *t*-test. In all cases, a two-tailed hypothesis analysis was performed, and a p-value below 0.05 was considered statistically significant. Sample size, statistical test, and p-value are denoted in results and figure legends.

3. Results

3.1. Bioinformatic analyses yielded a candidate for HEBE

To engineer a functional chimeric chronokine comprising the three human s-KL, sTREM2, and TIMP2 proteins, a comprehensive bioinformatic analysis was initially conducted to elucidate the structural characteristics of each protein, facilitating more accurate predictions. Subsequent insights into the conformational dynamics of the individual chronokines were gained through molecular dynamics (MD) simulations performed separately for each protein (Fig. 1A–E). Employing crystal structures as starting points, all-atom models were constructed, and a 520 ns trajectory was computed for each protein. Analysis of the root-mean-square deviations (RMSD) indicated that both s-KL and TIMP2 exhibited flexibility, evidenced by structural alterations compared to the reference crystal structure (Fig. S1A-C). Principal component analysis (PCA) facilitated the assessment of this conformational flexibility (Fig. 1B, D, F), revealing distinct conformational dynamics among the proteins. While sTREM2 displayed comparatively constrained dynamics (Fig. 1D), s-KL and TIMP2 explored broader conformational spaces, leading to diverse conformations during the simulations (Fig. 1B, E).

Root-mean-square fluctuations (RMSF) analysis identified the regions of highest flexibility within each protein structure (Fig. S1D-F), with protein structures color-coded based on the relative magnitude of fluctuations: from blue (low amplitude) to red (high amplitude) (Fig. 1A, C, E).

It was deduced that the flexibility observed in s-KL and TIMP2 might be linked to functional motions. Consequently, any efforts to combine these proteins should preserve their conformational freedom to prevent disruption of their respective functions.

Subsequently, models of the three proteins connected in a single polypeptide chain were constructed, with different protein distributions in the sequence and varying linkers being examined. Further MD simulations were conducted on these models to confirm that proteins would not aggregate and that each would maintain sufficient distance from the others to preserve conformational freedom.

Generally, more flexible linkers often resulted in aggregation or close proximity among the proteins. More favorable outcomes were achieved with rigid, helical linkers. The model with less frequent inter-protein contacts comprised sTREM2 + Linker1 + TIMP2 + Linker2 + s-KL (Fig. 1G). In this construct, Linker1 connected the C-terminal of sTREM2 to the N-terminal of TIMP2, while Linker2 replaced the 12 C-terminal residues of TIMP2 and connected to the N-terminal of s-KL. Linker1 consisted of 3 repeats of the sequence EAAAK, while Linker2 consisted of 5 repeats of the same sequence. The protein was designed for secretion, retaining the N-terminal signal peptide of sTREM2.

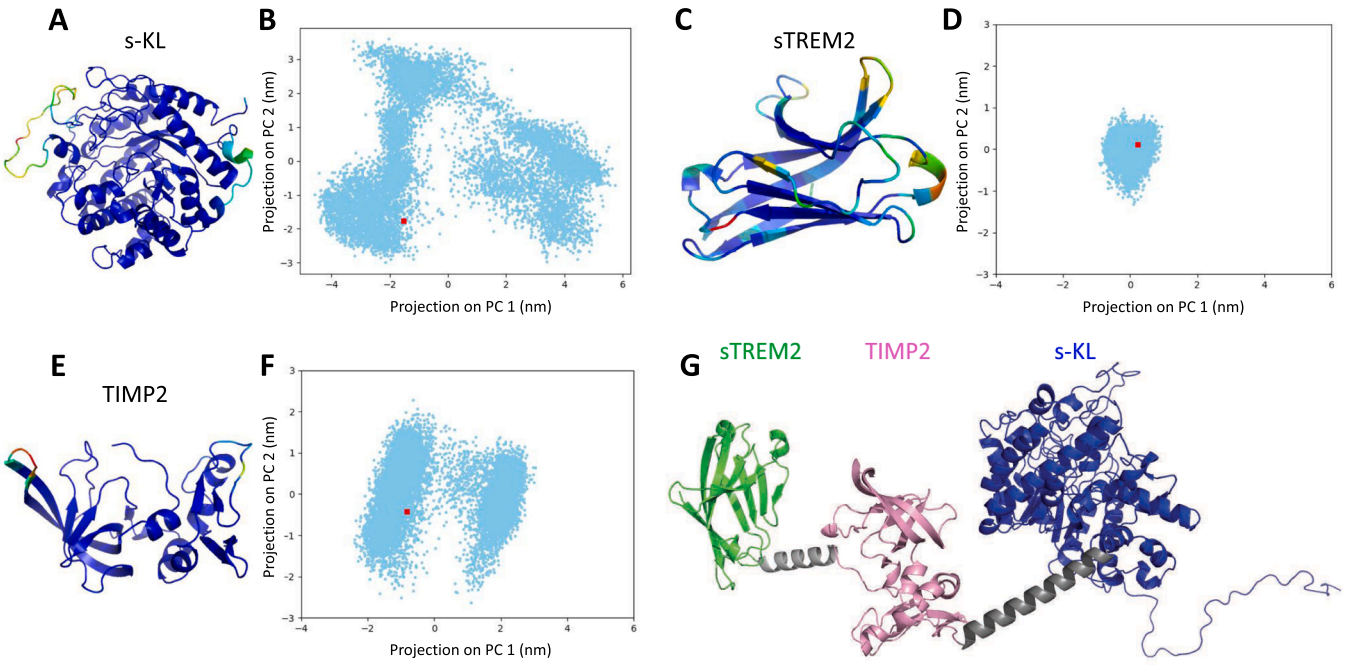

Fig. 1. Bioinformatic analysis to generate HEBE. Molecular dynamics of individual chronokines and HEBE model. (A, C, E) Structure of each protein colored by amplitude of the root-mean-square fluctuations (RMSF). The color scale ranges from blue (low amplitude fluctuations, greater rigidity) to red (high amplitude fluctuations, greater flexibility). (B, D, F) Principal component analysis (PCA). Projection of the trajectory of each protein in the space of the first two principal components. The red square denotes the crystal structure, used as the starting conformation of the simulation. Conformations visited in the trajectory are represented by blue dots. (G) Schematic representation of HEBE, comprised of the three individual chronokines and two EAAAK rigid linkers.

3.2. In vitro assays confirmed HEBE's stability and activity

To evaluate the stability of HEBE, a plasmid encoding the protein was constructed. The plasmid was then transfected into the HEK293 mammalian cell line, followed by Western Blot analysis, which detected a band approximately 130 kDa in size. This band was detected by antibodies against each of the subunits, indicating that the protein (i) is correctly expressed in cells, (ii) can be secreted by the cells, as evidenced by its presence in the supernatant, and (iii) does not undergo degradation at the junction of the linkers (Fig. 2A). Therefore, HEBE exhibits structural stability in an *in vitro* context.

However, to assess the *in vitro* efficacy of each individual subunit and consequently determine the functionality of the chimeric chronokine, recombinant proteins corresponding to each subunit were generated. The enzymatic activity of the s-KL subunit was evaluated using a β-glucuronidase assay (Fig. 2B). Interestingly, HEBE displayed significantly greater β-glucuronidase activity than s-KL alone, while neither of the other proteins exhibited this activity.

The effects of the sTREM2 subunit within HEBE were analyzed by measuring induction of phagocytic activity in the BV2 murine microglial cell line. Two fluorescent molecules, myelin and Aβ, were used as targets for phagocytosis. Given the increase in β-glucuronidase activity observed in HEBE compared to s-KL, a mixture of the three individual chronokines was also tested to assess any potential differences compared to HEBE. A flow cytometer was employed to quantify the phagocytosis of myelin or Aβ by BV2 cells, following a gating strategy represented in Fig. 2. After selecting the live cell population (Fig. 2C) and excluding aggregates (Fig. 2D), cell populations labeled with FITC, corresponding to phagocytosed myelin or Aβ (Fig. 2E), as well as CD45, indicative of microglial activation (Fig. 2F), were analyzed. Upon addition of myelin to the cell culture medium following treatment with recombinant proteins, more than half of the BV2 cells became activated, as indicated by an increase in the number of CD45 + cells (Fig. 2G). However, treatment with individual recombinant chronokines did not appear to influence this parameter. Despite the consistent level of cell activation observed across treatment groups, variations in phagocytic activity were evident. HEBE notably reduced the number of cells engaged in myelin phagocytosis, unlike the individual chronokines (Fig. 2H). Notably, HEBE displayed this effect despite the mixture of the three individual chronokines failing to do so, suggesting distinct behavior of HEBE compared to the chronokine mixture. Treatment with recombinant chronokines did not impact the degree of cell activation, as evidenced by consistent mean fluorescence in CD45 + cells across treatment groups (Fig. S2A). Moreover, the recombinant chronokines did not alter the amount of myelin phagocytosed per individual cell, as indicated by consistent mean myelin fluorescence per cell (Fig. S2B). Intriguingly, sTREM2 did not demonstrate the expected changes in myelin phagocytosis or BV2 cell activation under the tested conditions.

Upon addition of the Aβ peptide to the cell culture medium, distinct outcomes were observed compared to myelin. Firstly, a higher percentage of cells became activated, around 80 % (Fig. 2I), suggesting that under the tested conditions, Aβ is a greater activator of BV2 compared to myelin. Treatment with individual recombinant chronokines also influenced cell activation in the presence of Aβ. Specifically, s-KL slightly decreased the number of activated cells, whereas HEBE increased it. Additionally, the mixture of the three chronokines also decreased the number of activated cells. Importantly, similar to the observations with myelin, HEBE exhibited unique activity compared to the mixture of individual proteins, further confirming distinct behavior of HEBE from the chronokine mixture. The decrease in the number of activated cells observed with sKL and the mixture was accompanied by a reduction in the number of cells phagocytosing Aβ, while HEBE did not appear to affect this parameter despite the slight increase in the number of activated cells (Fig. 2J). However, due to the high percentage of activated cells following incubation with Aβ, detecting significant effects on activation and phagocytosis mediated by HEBE proved challenging. Interestingly, although the activation level of CD45+ cells was not significantly altered (Fig. S2C), all treatments with chronokines

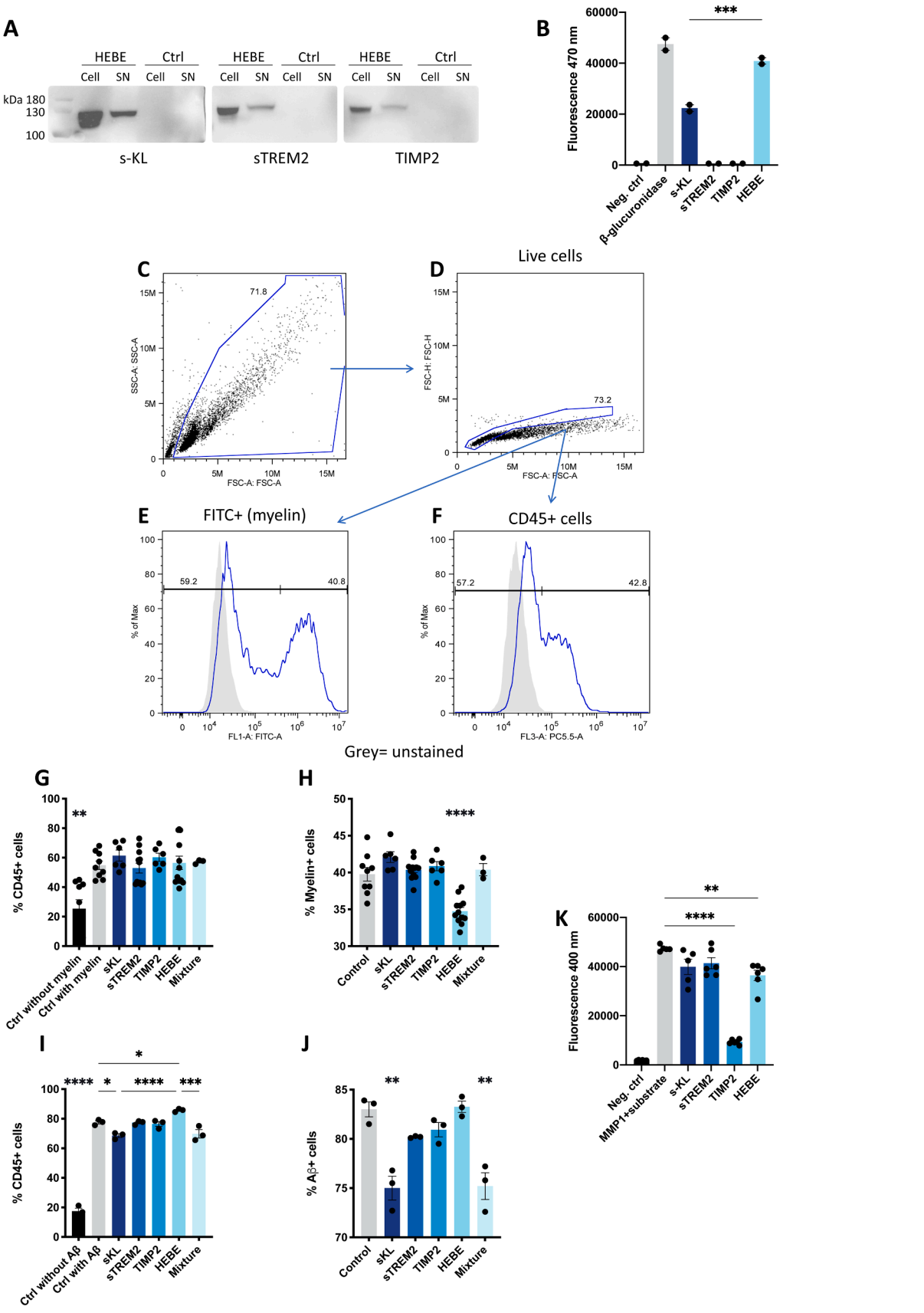

(caption on next page)

Fig. 2. HEBE shows biological activity in in vitro functional characterization. (A) Western Blot of HEK293 cells transfected with a plasmid encoding HEBE or Null. Both cell lysates (Cell) and supernatants (SN) were loaded, and the immunodetection was performed using antibodies against each of the subunits as indicated below each membrane. Theoretical molecular weight of HEBE is 100 kDa. (B) β-glucuronidase activity assay. 10 μg of s-KL and equimolar amounts of the other proteins were used with two replicates per condition. Bovine β-glucuronidase was used as a positive control, while the negative control did not contain any protein. (C) Forward and side scatter density plot of the whole BV2 cell population. (D) Forward scatter height versus forward scatter area density plot of live BV2 cells. (E) FITC positive BV2 cell histogram. (F) CD45 positive BV2 cell histogram. (G) Percentage of BV2 cells with positive CD45 labeling in the myelin phagocytosis assay. (H) Percentage of BV2 cells with phagocytosed myelin. (I) Percentage of BV2 cells with positive CD45 labeling in the Aβ phagocytosis assay. (J) Percentage of BV2 cells with phagocytosed Aβ⊡ (K) MMP1 inhibition activity assay. 0.8 μg/mL of TIMP2 and equimolar amounts of the other proteins were used with six replicates per condition. Only the substrate was used as a negative control, while no TIMP2 was added as a control for the enzymatic reaction. Data are shown as Mean ± SEM, One-way ANOVA and Tukey post-hoc (*p < 0.05, **p < 0.01, ***p < 0.001, ****p < 0.0001).

appeared to decrease the amount of Aβ phagocytosed per cell compared to control cells (Fig. S2D). Moreover, once again, sTREM2 did not present functions different from the other chronokines.

An enzymatic assay was employed to assess the activity of the TIMP2 subunit. In this assay, activity is measured through a decrease in the fluorescence of the product of the FS-6 fluorogenic substrate resulting from the inhibition of MMP1 by TIMP2. It is noteworthy that TIMP2 alone demonstrated potent efficacy in inhibiting MMP1 (Fig. 2K), leading to a notable reduction in fluorescence compared to the control lacking TIMP2. In contrast, neither s-KL, sTREM2, nor HEBE exhibited any inhibitory effect on MMP1.

3.3. *In vivo gene therapy study with HEBE achieved long-term expression of the chimeric chronokine*

To explore the potential protective effects of HEBE in an AD mouse model, we used a double APP/Tau transgenic model that develops both amyloid and Tau pathologies and hippocampal-dependent memory deficits at 6 months of age [24]. At 24 weeks of age, these transgenic mice were administered intravenous injections of an AAV9P31 viral vector expressing either HEBE or a non-coding Null sequence, serving as a control (Fig. S3A). The AAV9P31 viral vector was selected for its ability to efficiently cross the murine blood-brain barrier [32]. Twelve weeks post-injection, a series of behavioral and memory tests were conducted on both male and female mice. Subsequently, euthanasia was performed, and tissue samples were collected for further analysis. Quantitative PCR confirmed the expression of the HEBE viral vector in both liver and brain tissues. However, it is noteworthy that expression levels in the liver of female mice were significantly lower compared to male counterparts, consistent with previous observations using AAV vectors (Fig. S3B-E) [36]. Importantly, a thorough analysis of blood samples from WT mice injected with HEBE did not reveal any evidence of toxic effects (Figs. S4,5).

3.4. *HEBE improves behavior and memory in AD mice*

To evaluate locomotor activity and anxiety-like behaviors, we conducted an Open Field test (Fig. 3). Analysis showed no significant differences in terms of traveled distance and mean speed between male and female mice. At 36 weeks of age, both male and female AD mice

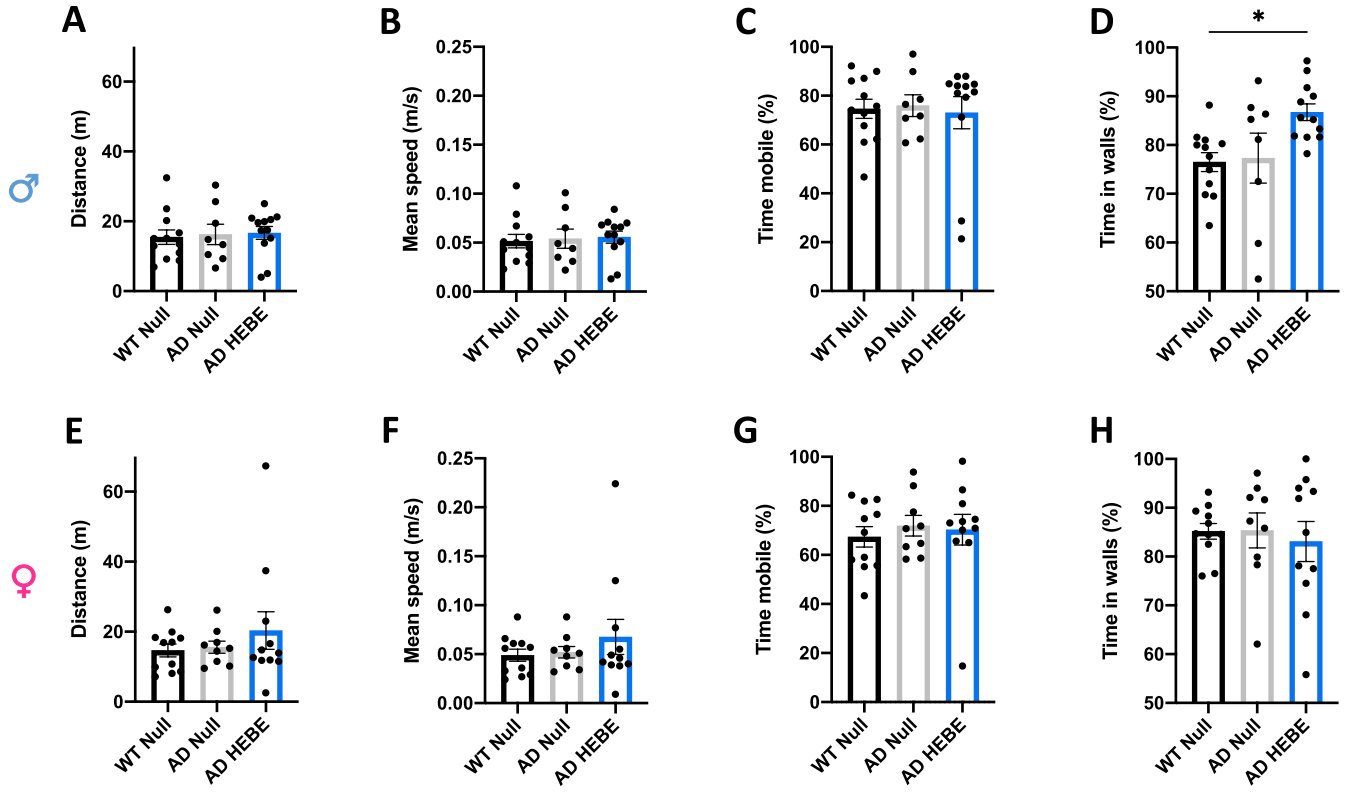

Fig. 3. Locomotor activity in APP/Tau mice was unaffected by HEBE, but anxiety was moderately increased in males. (A, E) Distance travelled in the Open Field. (B, F) Mean speed in the Open Field. (C, G) Percentage of time mice spent mobile during the test. (D, H) Percentage of time mice spend around the walls of the Open Field. Data are shown as Mean ± SEM, One-way ANOVA and Tukey post-hoc (*p < 0.05). Sample size after discarding outliers for males: WT-Null= 12, AD-Null= 8, AD-HEBE= 12. Sample size for females: WT-Null= 11, AD-Null= 9, AD-HEBE= 11.

exhibited normal locomotor activity, and the treatment did not have any observable effects on this parameter (Fig. 3A, B, E, F). Anxiety levels were assessed by analyzing the percentage of time spent in motion, as immobility can indicate fear. No sex-related differences were observed in the duration of movement (Fig. 3C, G). Thigmotaxis, the tendency of mice to remain close to the walls, was also measured as an indicator of anxiety-like behavior. While no differences were observed in females (Fig. 3H), a slight increase in thigmotaxis was observed in males treated with HEBE compared to WT mice (Fig. 3D). Overall, these findings suggest that mice did not display locomotor impairments, although males treated with HEBE may exhibit mild increases in anxiety-like behaviors.

Recognition memory performance was evaluated using a Novel Object Recognition Test (Fig. 4). Initially, mice displayed no significant preference for any of the identical objects on the first day of testing (Fig. 4A, E). However, on the subsequent day, when one of the objects was replaced with a novel item, differences in the preference index were observed, despite non-significant variations in object exploration time (Fig. 4C, G). AD-Null mice exhibited no preference for the new object, suggesting a lack of memory retention from the previous day's exploration (Fig. 4B, F). In contrast, HEBE-treated mice displayed a preference for the new object, reaching levels comparable to those of WT mice, albeit without statistical significance in male mice. Nonetheless, these results collectively suggest a potential enhancement in memory when AD mice are treated with HEBE. Comparisons of preference indexes between the first and second days revealed improvements in both WT and HEBE-treated mice, while no such changes were observed in the AD group treated with Null (Fig. 4D, H). These findings indicate an improvement in recognition memory when AD mice receive HEBE treatment.

HEBE's impact on hippocampal-dependent spatial learning was investigated using the Morris Water Maze. WT mice consistently demonstrated better performance throughout all testing days with the hidden target platform. However, both AD groups displayed prolonged latencies to reach the platform on the first day of testing (Fig. 5A, C). Despite this initial disparity in performance among the groups, HEBE-treated mice exhibited a gradual improvement in their ability to locate the target platform across successive training days ($p = 0.03$ for males, $p = 0.005$ for females), eventually achieving latencies comparable to those of WT mice by the final day of training. In contrast, Null-treated AD mice did not show any noticeable enhancement in performance over time. A similar trend of improvement was observed in the number of entries to the target platform throughout the study duration (Fig. 5B, D). While WT mice performed consistently well from the first day, only HEBE-treated mice displayed a significant improvement ($p = 0.02$ for males, $p = 0.005$ for females). AD mice did not exhibit a learning curve in locating the target platform. These findings suggest that HEBE enhances hippocampal-dependent spatial learning in AD mice.

3.5. Phosphorylated Tau is reduced after HEBE treatment

Given that two prominent hallmarks of AD are the accumulation of Aβ in plaques and phosphorylated Tau (pTau) in neurofibrillary tangles, we conducted an analysis of these pathological markers in the brains of mice using immunofluorescence imaging. Our focus was primarily on the hippocampus, a brain region essential for memory and learning and affected early in AD.

In terms of pTau, it was not detected in WT mice, as anticipated (Fig. 6A–E). However, significant levels of pTau were observed in pyramidal and granular neurons in AD mice, irrespective of gender or hippocampal subregion. Notably, this heightened pTau signal was attenuated in HEBE-treated mice, suggesting a beneficial effect of the treatment. It is noteworthy that females exhibited lower levels of pTau (Fig. 6C, E) compared to males (Fig. 6B, D).

As for Aβ, WT mice exhibited minimal or no presence of the amyloid peptide (Fig. 7A-E). In contrast, AD mice displayed elevated levels of Aβ,

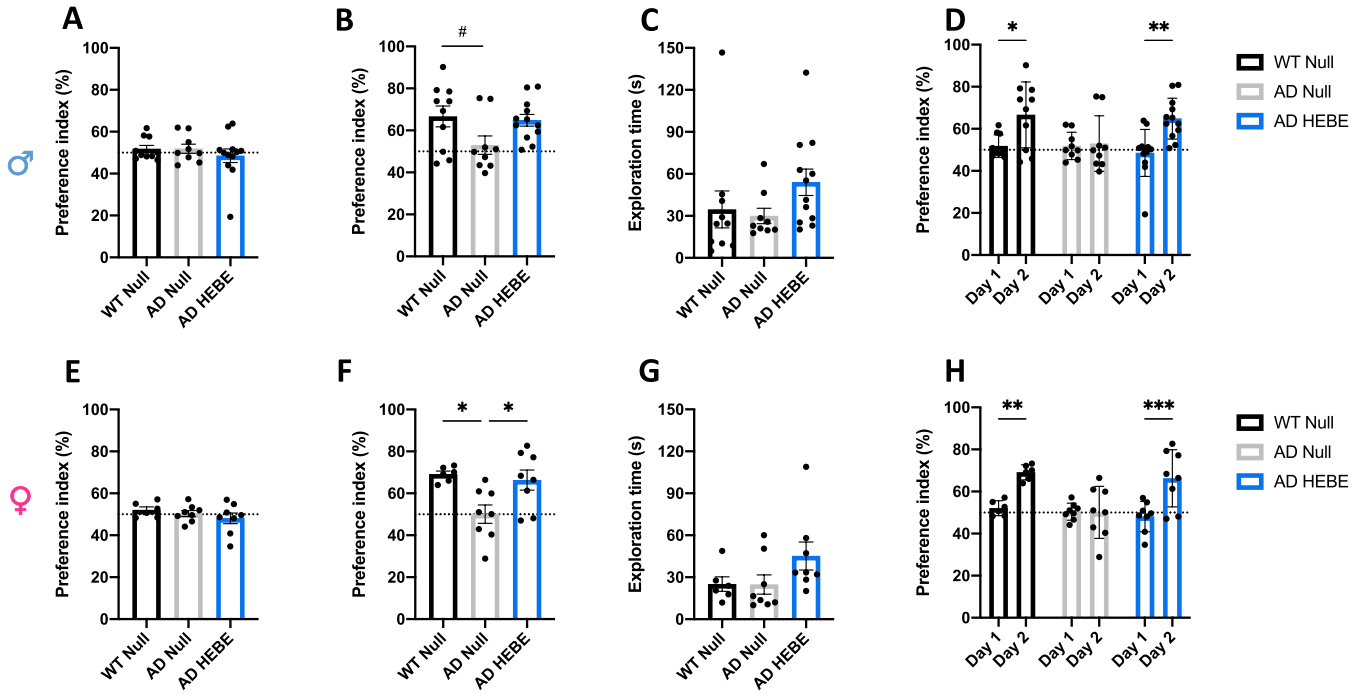

Fig. 4. Recognition memory is improved in APP/Tau mice treated with HEBE in the Novel Object Recognition Test. (A, E) Preference index the first day of the test, when both objects are identical. (B, F) Preference index for the new object the second day of the test. (C, G) Total time mice spent exploring the objects. (D, H) Comparison of the preference index between the two days of the test. Data are shown as Mean ± SEM, One-way ANOVA and Tukey post-hoc, comparisons between days analyzed by 2-way ANOVA and Tukey post-hoc (*$p < 0.05$, **$p < 0.01$, ***$p < 0.001$, #<0.07). Sample size after discarding outliers for males: WT-Null= 10, AD-Null= 9, AD-HEBE= 12. Sample size for females: WT-Null= 6, AD-Null= 9, AD-HEBE= 9.

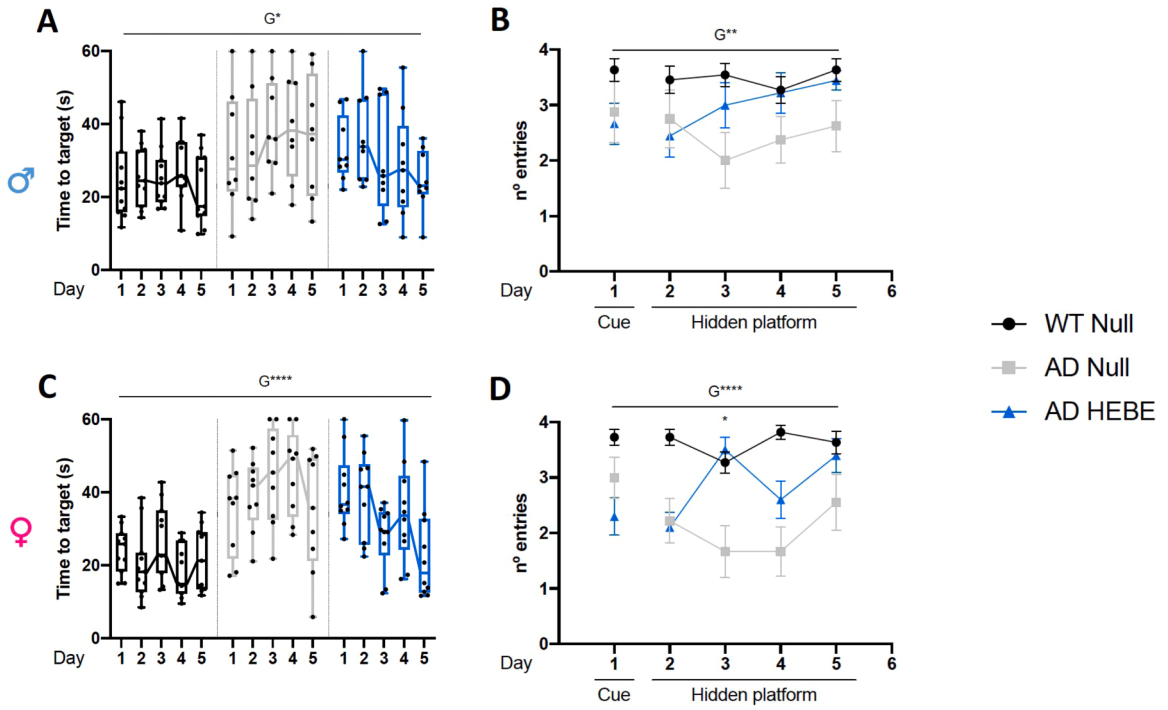

Fig. 5. HEBE improves spatial learning in APP/Tau mice in the Morris Water Maze. (A, C) Time to reach the target platform inside the pool. (B, D) Average number of entries to the platform on each training day. Data are shown as Mean ± SEM, 2-way ANOVA and Tukey post-hoc (*p < 0.05, **p < 0.01, ***p < 0.001, ****p < 0.0001). G: group factor. Sample size after discarding outliers for males: WT-Null = 11, AD-Null = 8, AD-HEBE = 9. Sample size for females: WT-Null = 11, AD-Null = 9, AD-HEBE = 10.

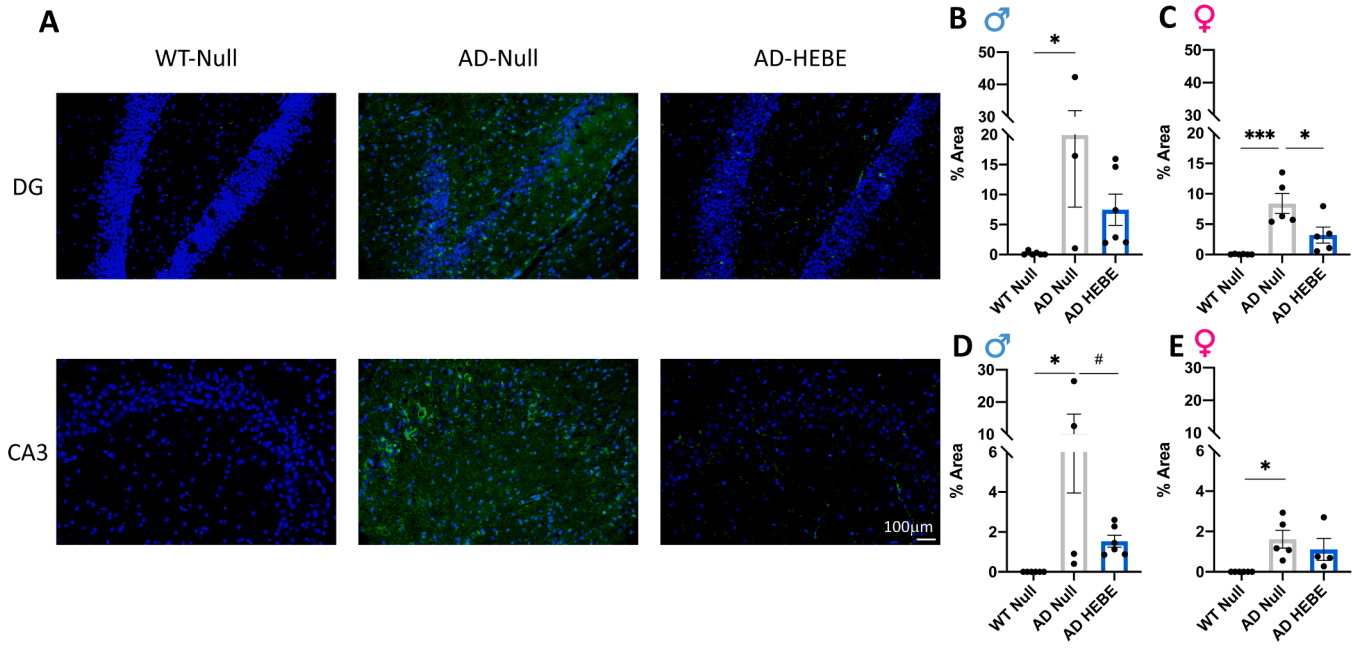

Fig. 6. HEBE attenuates pTau levels in the hippocampus of APP/Tau mice. (A) Representative images for each group. Green: pTau labeling, blue: DAPI. (B, C) Quantification of positive pTau area in the dentate gyrus, in males and females, respectively. (D, E) Quantification of positive pTau area in the CA3 region, in males and females, respectively. Data are shown as Mean ± SEM of 2 sections per animal, One-way ANOVA and Tukey post-hoc (*p < 0.05, ***p < 0.001, #<0.1). *T*-test for comparisons of means within groups among test days. Sample size for males: WT-Null = 6, AD-Null = 5, AD-HEBE = 6. Sample size for females: WT-Null = 6, AD-Null = 5, AD-HEBE = 5.

although the treatment did not seem to substantially influence these levels. A slight trend towards reduction was observed in the dentate gyrus of HEBE-treated males (Fig. 7B) and the CA3 region in HEBE-treated females (Fig. 7E), albeit without reaching statistical significance.

4. Discussion

Until recently, the therapeutic options available for Alzheimer's disease provided symptomatic relief without addressing the underlying

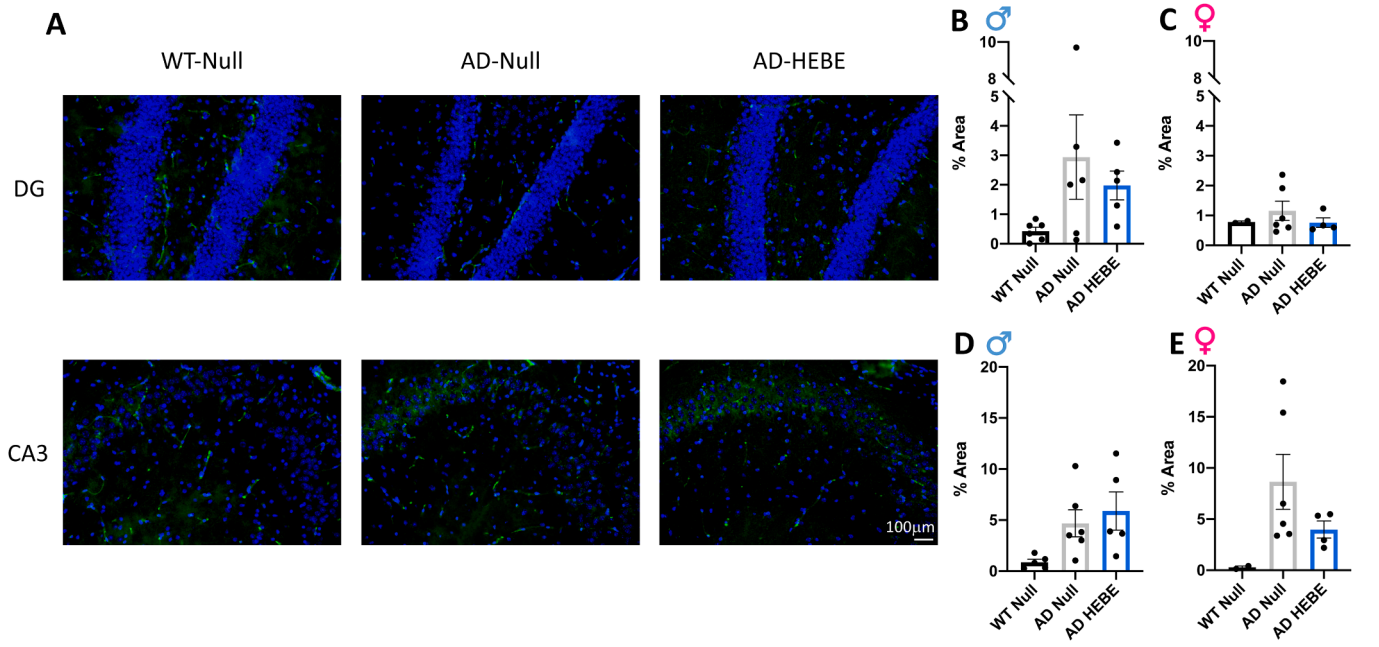

Fig. 7. HEBE does not significantly impact β-amyloid levels in APP/Tau mice. (A) Representative images for each group. Green: β-amyloid labeling, blue: DAPI. (B, C) Quantification of positive Aβ area in the dentate gyrus, in males and females, respectively. (D, E) Quantification of positive Aβ area in the CA3 region, in males and females, respectively. Data are shown as Mean ± SEM of 2 sections per animal, One-way ANOVA and Tukey post-hoc. Sample size for males: WT-Null = 6, AD-Null = 5, AD-HEBE = 5. Sample size for females: WT-Null = 2, AD-Null= 6, AD-HEBE = 4.

biological mechanisms driving the pathology [37]. In recent years, however, disease-modifying treatments have gained interest due to their potential to ameliorate the biological processes implicated in AD, improving treatment outcomes. Predominantly, clinical trials using disease-modifying treatments focus on modulating the Aβ biological pathway, based on the already disputed amyloid cascade hypothesis [38,39]. Notably, the FDA has only approved two disease-modifying treatments, namely lecanemab [40] and aducanumab [41], which are monoclonal antibodies aimed at inhibiting amyloid aggregation. However, a significant limitation of these treatments lies in the targeting of a specific pathway, overlooking the complexity of the disease [42], and resulting in limited clinical efficacy. The lack of a broader targeting is one of the reasons many of the treatments in clinical trials do not achieve approval by regulatory agencies [38,43].

Since AD is a complex disease characterized by the dysregulation of numerous pathways we believe that using pleiotropic chronokines capable of simultaneously improving multiple mechanisms could offer greater therapeutic potential for the treatment of AD. In this context, we introduce HEBE, a novel chimeric protein developed by combining three carefully selected chronokines, each addressing distinct aspects of AD pathology, and it also provide a foundational exploration of its therapeutic potential. Through this work, we observed significant benefits supporting the hypothesis that HEBE exerts a neuroprotective effect. The development of HEBE was guided by a comprehensive bioinformatic analysis aimed at evaluating each chronokine individually to minimize conformational alterations while preserving their functionality when combined. Given the complexity of these analyses, human versions of these proteins were chosen for translatability to humans, as each individual human chronokine has been shown to function in mice [17,20,44]. Previous studies had only assessed the structure and flexibility for the sTREM2 protein [45], yielding RMSD and RMSF plots similar to those observed in our study, and confirming the limited flexibility of the protein. In contrast, studies on s-KL and TIMP2 had primarily explored their structures and flexibilities within the context of protein-protein interactions. For example, studies on Klotho have centered on its full-length structure when interacting with either FGF23 [46,47] or VEGFR2 and TRCP1 [48]. Similarly, previous examinations of TIMP2 did not assess its flexibility upon crystal structure determination [49], and subsequent studies have focused on its interactions with matrix metalloproteinases [50,51]. To our knowledge, this study represents the first comprehensive analysis of s-KL and TIMP2 structures and flexibilities. Our analysis revealed that both chronokines are flexible, a trait likely crucial for their functional roles. To preserve their conformational freedom, rigid linkers were introduced between the proteins to spatially separate them, mitigating potential interactions and aggregation. Subsequent attempts yielded a soluble HEBE variant devoid of aggregation, confirmed via *in vitro* stability analysis.

Further *in vitro* investigations employing recombinant proteins were conducted to ascertain whether HEBE maintained the functionalities of each individual chronokine. Initially, we observed that HEBE preserved the β-glucuronidase activity of s-KL, displaying even greater activity than s-KL alone. Subsequently, analysis of phagocytic activity associated with sTREM2 in BV2cells revealed that HEBE's impact on phagocytosis varied depending on the targeted molecule to be phagocytosed. Specifically, HEBE led to a reduction in myelin phagocytosis, whereas it did not affect Aβ phagocytosis. Additionally, a moderate increase in cell activation was observed upon HEBE addition, although this did not translate into enhanced phagocytic activity. The limited effects observed with Aβ could be attributed to the already high cell activation state in the presence of Aβ, making it challenging to discern further increases in phagocytic activity. Unfortunately, contrary to previous findings [17,52], neither commercial recombinant sTREM2 proteins nor our in-house-produced protein showed alterations in phagocytic activity in our experiments. Hence, in the absence of a working control for our test, we cannot confirm sTREM2's function on phagocytosis modulation. Some studies indicate that sTREM2 may have greater impact on the activation of microglia and inflammatory responses rather than phagocytic activity [53–55], unlike the transmembrane form of the protein. Therefore, conducting a comprehensive analysis of microglial activation in future experiments could provide insights into sTREM2's mechanisms of action. Furthermore, s-KL's unexpected effect of reducing phagocytic activity in the presence of Aβ has not been previously described to our knowledge. Despite differences depending on the phagocytosed molecule, a consistent and noteworthy conclusion emerged: HEBE exhibited

distinct activity compared to the mixture of individual chronokines. This suggests that the conformation resulting from the union of the three proteins could enhance existing functions or confer new ones, potentially increasing HEBE's therapeutic potential compared to the administration of the three chronokines individually. Furthermore, the capacity of HEBE to inhibit MMP1 associated with TIMP2 was investigated, revealing lower inhibition levels compared to TIMP2 alone. Nevertheless, HEBE may retain other functions [21] that could contribute to the amelioration of AD pathology.

To test the *in vivo* effects of HEBE, we used a double APP/Tau transgenic mouse model that expresses mutant human APP and Tau in glutamatergic neurons and recapitulates amyloid and Tau pathologies, along with memory deficits [24]. Treatment was initiated at 24 weeks of age, corresponding to the onset of initial symptoms, and behavioral and memory assessment were performed at 36 weeks, representing a advanced stage of pathology. The study aimed to evaluate HEBE's potential to slow the progression of pathology following symptom onset.

For the *in vivo* proof of concept, a gene therapy approach utilizing viral vectors was adopted for its ability to ensure long-term transgene expression and efficient brain cell transduction. AAV9P31, a variant of AAV9, was selected due to its capacity to cross the blood-brain barrier in mice [32], enabling non-invasive intravenous vector administration. This approach facilitated uniform vector distribution throughout the central nervous system, particularly in the hippocampus, a crucial region affected in AD. Additionally, the vector's liver tropism facilitates protein secretion into the bloodstream, potentially inducing peripheral effects mediated by HEBE, which may contribute to ameliorating the pathology.

In vivo experiments were conducted to evaluate the effects of HEBE on both general behavior and memory performance. Initially, the Open Field study showed no impact of HEBE on sensorimotor abilities but a slight increase in anxiety, particularly in males. However, females did not exhibit increased thigmotaxis, although both WT and AD groups showed some degree of wall-seeking behavior, indicative of some anxiety. Nevertheless, this anxiety effect did not significantly influence other parameters examined in these animals.

Memory performance was assessed using the Novel Object Recognition test, revealing significant improvement in object recognition in both male and female AD mice treated with HEBE, reaching levels comparable to WT mice. These results align with previous studies demonstrating cognitive enhancement with individual chronokines [7,56,57]. Additionally, an amelioration in spatial learning was evident in the Morris Water Maze assessment. During the learning phase, untreated AD mice exhibited deficient task acquisition, as evidenced by prolonged latency to reach the platform and diminished entries. In contrast, HEBE-treated cohorts demonstrated enhanced spatial learning, reaching the levels of WT mice by the last learning day. Overall, these data indicate HEBE's efficacy in mitigating hippocampus-dependent learning and memory deficits in the APP/Tau murine model.

Immunofluorescence analysis of mouse brains revealed alterations in the levels of key Alzheimer's pathology proteins such as Aβ and pTau. HEBE treatment reduced levels of hyperphosphorylated Tau protein, similarly to previous studies with Klotho and sTREM2 [58,59]. Furthermore, there was a trend towards lower Aβ levels in the hippocampus with HEBE treatment, though not statistically significant. Further research is needed to confirm HEBE's effects on Aβ clearance, potentially through augmenting microglial phagocytosis as suggested by literature on sTREM2 [60–62].

Since this investigation focused on the prodromal phase, further studies are required to assess HEBE's therapeutic efficacy in more advanced disease stages. Moreover, although this study primarily focuses on the design and initial analysis of the therapeutic potential of HEBE, recent efforts have been initiated to delineate the specific roles of its individual components—s-KL, sTREM2, and TIMP2—and to explore whether their effects are independent or arise from a synergistic interaction. These ongoing studies will provide deeper insights into the mechanisms underlying HEBE's actions, which will be addressed in future publications.

In conclusion, the development of HEBE represents a promising step forward in the treatment of neurodegenerative disorders. While further investigations are needed to elucidate its underlying mechanisms and optimize its application, the findings presented here establish a strong foundation for its therapeutic potential and pave the way for future studies to expand on these initial observations.

CRediT authorship contribution statement

Assumpció Bosch: Writing – review & editing, Conceptualization. **David Ramirez-Gomez:** Investigation. **Carlos Alberto Saura:** Writing – review & editing, Resources. **Beatriz Almolda:** Writing – review & editing, Investigation, Formal analysis, Conceptualization. **Maria Dolores Capilla-López:** Investigation. **Pedro Renault:** Methodology, Investigation, Formal analysis, Conceptualization. **Rebeca Blanch:** Investigation. **Ángel Edo:** Investigation. **Jesús Giraldo:** Writing – review & editing, Resources. **Jon Esandi:** Writing – original draft, Visualization, Methodology, Investigation, Formal analysis, Conceptualization. **Miguel Chillon:** Writing – review & editing, Visualization, Supervision, Project administration, Methodology, Funding acquisition, Conceptualization.

Declaration of Generative AI and AI-assisted technologies in the writing process

During the preparation of this work the authors used ChatGPT in order to improve readability and language. After using this tool, the authors reviewed and edited the content as needed and takes full responsibility for the content of the publication.

Funding

This work was funded by MICINN/AEI/10.13039/501100011033 (PID2022–142624OB-I00 and PID2019–104034RB-I00 to MC); (PID2022-137668OB-I00) to CS; and (PID2023–148834OB-I00) to AB; by Instituto de Salud Carlos III and NexGenerationEU (RICORS, RD21/0017/0008) to MC and AB; and Generalitat de Catalunya (2021SGR-00529) to AB and MC, and (2021SGR-00142) to CS. JE was a recipient of a fellowship by the Generalitat de Catalunya (2020FI-SDUR0037). DRG was a recipient of a VHIR Fellowship. RB was a recipient of a fellowship by the Gobierno de España (FPU16/03137). MDCL was a recipient of a fellowship by the Ministerio de Ciencia e Innovación (BES-2017-082072).

Declaration of Competing Interest

The authors declare the following financial interests/personal relationships which may be considered as potential competing interests: Portions of this work are the subject of a patent application held by the Universitat Autònoma de Barcelona (UAB, Spain); the Institució Catalana de Recerca i Estudis Avançats (ICREA, Spain); and the Vall d'Hebron Institute of Research (VHIR, Spain). J.E., P.R., A.B., B.A., J.G., and M.C. are included in this patent application. No other authors possess a conflict of interest.

Appendix A. Supporting information

Supplementary data associated with this article can be found in the online version at doi:10.1016/j.biopha.2025.117815.

Data availability

Data will be made available on request.

References

[1] 2023 Alzheimer's disease facts and figures, Alzheimer's & Dementia 19(4), 2023, pp. 1598–1695.
[2] D.J. Selkoe, J. Hardy, The amyloid hypothesis of Alzheimer's disease at 25 years, EMBO Mol. Med. 8 (2016) 595–608.
[3] A. Serrano-Pozo, M.P. Frosch, E. Masliah, B.T. Hyman, Neuropathological alterations in Alzheimer disease, Cold Spring Harb. Perspect. Med. 1 (2011) a006189.
[4] D.M. Holtzman, J.C. Morris, A.M. Goate, Alzheimer's disease: the challenge of the second century, Sci. Transl. Med. 3 (77) (2011) 77sr1.
[5] V. Kheifets, S.P. Braithwaite, Plasma-based strategies for therapeutic modulation of brain aging, Neurotherapeutics 16 (2019) 675–684.
[6] A. Massó, A. Sánchez, A. Bosch, L. Giménez-Llort, M. Chillón, Secreted αKlotho isoform protects against age-dependent memory deficits, Mol. Psychiatry 23 (2018) 1937–1947.
[7] J. Roig-Soriano, C. Griñán-Ferré, J.F. Espinosa-Parrilla, C.R. Abraham, A. Bosch, M. Pallàs, M. Chillón, AAV-mediated expression of secreted and transmembrane αKlotho isoforms rescues relevant aging hallmarks in senescent SAMP8 mice, Aging Cell 21 (2022) e13581.
[8] B.A. Baldo, Chimeric fusion proteins used for therapy: indications, mechanisms, and safety, Drug Saf. 38 (2015) 455–479.
[9] D. Sun, X. Shi, S. Li, X. Wang, X. Yang, M. Wan, CAR-T cell therapy: a breakthrough in traditional cancer treatment strategies (Review), Mol. Med Rep. 29 (2024) 47.
[10] M. Kuro-O, Y. Matsumura, H. Aizawa, H. Kawaguchi, T. Suga, T. Utsugi, Y. Ohyama, M. Kurabayashi, T. Kaname, E. Kumek, H. Iwasakik, A. Iida, T. Shiraki-Iida, S. Nishikawa, R. Nagai, N. Yo-Ichi, Mutation of the mouse klotho gene leads to a syndrome resembling ageing, Nature 390 (6655) (1997) 45–51.
[11] T. Nagai, K. Yamada, H.C. Kim, Y.S. Kim, Y. Noda, A. Imura, Y. ichi Nabeshima, T. Nabeshima, Cognition impairment in the genetic model of aging klotho gene mutant mice: a role of oxidative stress, FASEB J. 17 (2003) 50–52.
[12] M. Shiozaki, K. Yoshimura, M. Shibata, M. Koike, N. Matsuura, Y. Uchiyama, T. Gotow, Morphological and biochemical signs of age-related neurodegenerative changes in klotho mutant mice, Neuroscience 152 (2008) 924–941.
[13] A. Uchida, Y. Komiya, T. Tashiro, H. Yorifuji, T. Kishimoto, Y. Nabeshima, S.-I. Hisanaga, Neurofilaments of klotho, the mutant mouse prematurely displaying symptoms resembling human aging, J. Neurosci. Res 64 (2001) 364–370.
[14] Y. Matsumura, H. Aizawa, T. Shiraki-Iida, R. Nagai, M. Kuro-O, Y.-I. Nabeshima, Identification of the Human Klotho Gene and Its Two Transcripts Encoding Membrane and Secreted Klotho Protein, Biochem Biophys. Res Commun. 242 (1998) 626–630.
[15] D. Feuerbach, P. Schindler, C. Barske, S. Joller, E. Beng-Louka, K.A. Worringer, S. Kommineni, A. Kaykas, D.J. Ho, C. Ye, K. Welzenbach, G. Elain, L. Klein, I. Brzak, A.K. Mir, C.J. Farady, R. Aichholz, S. Popp, N. George, U. Neumann, ADAM17 is the main sheddase for the generation of human triggering receptor expressed in myeloid cells (hTREM2) ectodomain and cleaves TREM2 after Histidine 157, Neurosci. Lett. 660 (2017) 109–114.
[16] T.R. Jay, V.E. Von Saucken, G.E. Landreth, TREM2 in neurodegenerative diseases, Mol. Neurodegener. 12 (1) (2017) 56.
[17] L. Zhong, Y. Xu, R. Zhuo, T. Wang, K. Wang, R. Huang, D. Wang, Y. Gao, Y. Zhu, X. Sheng, K. Chen, N. Wang, L. Zhu, D. Can, Y. Marten, M. Shinohara, C.C. Liu, D. Du, H. Sun, L. Wen, H. Xu, G. Bu, X.F. Chen, Soluble TREM2 ameliorates pathological phenotypes by modulating microglial functions in an Alzheimer's disease model, Nat. Commun. 10 (1) (2019) 1365.
[18] K.D. Belsare, H. Wu, D. Mondal, A. Bond, E. Castillo, J. Jin, H. Jo, A.E. Roush, K. Bharath Pilla, A. Sali, C. Condello, W.F. Degrado, Soluble TREM2 inhibits secondary nucleation of Aβ fibrillization and enhances cellular uptake of fibrillar Aβ, Biophys. Comput. Biol. 119 (5) (2022) e2114486119.
[19] C.F. Slattery, J.A. Beck, L. Harper, G. Adamson, Z. Abdi, J. Uphill, T. Campbell, R. Druyeh, C.J. Mahoney, J.D. Rohrer, J. Kenny, J. Lowe, K.K. Leung, J. Barnes, S. L. Clegg, M. Blair, J.M. Nicholas, R.J. Guerreiro, J.B. Rowe, C. Ponto, I. Zerr, H. Kretzschmar, P. Gambetti, S.J. Crutch, J.D. Warren, M.N. Rossor, N.C. Fox, J. Collinge, J.M. Schott, S. Mead, R47H TREM2 variant increases risk of typical early-onset Alzheimer's disease but not of prion or frontotemporal dementia, Alzheimer's Dement. 10 (2014) 602–608.e4.
[20] J.M. Castellano, K.I. Mosher, R.J. Abbey, A.A. McBride, M.L. James, D. Berdnik, J. C. Shen, B. Zou, X.S. Xie, M. Tingle, I.V. Hinkson, M.S. Angst, T. Wyss-Coray, Human umbilical cord plasma proteins revitalize hippocampal function in aged mice, Nature 544 (2017) 488–492.
[21] R. Britton, T. Wasley, R. Harish, C. Holz, J. Hall, D.C. Yee, J.M. Witt, E.A. Booth, S. Braithwaite, E. Czirr, M.K. Campbell, Noncanonical activity of tissue inhibitor of metalloproteinases 2 (TIMP2) improves cognition and synapse density in aging, ENeuro 10 (6) (2023), 0031-23.2023.
[22] L. Pérez-Martínez, D.M. Jaworski, Tissue inhibitor of metalloproteinase-2 promotes neuronal differentiation by acting as an anti-mitogenic signal, J. Neurosci. 25 (2005) 4917–4929.
[23] D.-W. Seo, H. Li, L. Guedez, P.T. Wingfield, T. Diaz, R. Salloum, B.-Y. Wei, W. G. Stetler-Stevenson, TIMP-2 mediated inhibition of angiogenesis: an MMP-independent mechanism, Cell 114 (2003) 171–180.
[24] M.D. Capilla-López, A. Deprada, Y. Andrade-Talavera, I. Martínez-Gallego, H. Coatl-Cuaya, J. Rodríguez-Alvarez, A. Rodríguez-Moreno, A. Parra-Damas, C.A. Saura, Differential neural circuit vulnerability to β-amyloid and tau pathologies in novel Alzheimer's disease mice, BioRxiv (2023).
[25] B. Webb, A. Sali, Comparative protein structure modeling using MODELLER, Curr. Protoc. Bioinforma. 2016 (2016) 5.6.1–5.6.37.
[26] S. Doerr, M.J. Harvey, F. Noé, G. De Fabritiis, HTMD: high-throughput molecular dynamics for molecular discovery, J. Chem. Theory Comput. 12 (2016) 1845–1852.
[27] J.A. Maier, C. Martinez, K. Kasavajhala, L. Wickstrom, K.E. Hauser, C. Simmerling, ff14SB: improving the accuracy of protein side chain and backbone parameters from ff99SB, J. Chem. Theory Comput. 11 (2015) 3696–3713.
[28] W.L. Jorgensen, J. Chandrasekhar, J.D. Madura, R.W. Impey, M.L. Klein, Comparison of simple potential functions for simulating liquid water, J. Chem. Phys. 79 (1983) 926–935.
[29] M.J. Harvey, G. Giupponi, G.De Fabritiis, ACEMD: accelerating biomolecular dynamics in the microsecond time scale, J. Chem. Theory Comput. 5 (2009) 1632–1639.
[30] M.J. Abraham, T. Murtola, R. Schulz, S. Páll, J.C. Smith, B. Hess, E. Lindah, Gromacs: High performance molecular simulations through multi-level parallelism from laptops to supercomputers, SoftwareX 1–2 (2015) 19–25.
[31] S. Jo, T. Kim, V.G. Iyer, W. Im, CHARMM-GUI: a web-based graphical user interface for CHARMM, J. Comput. Chem. 29 (2008) 1859–1865.
[32] D.H. De Jong, G. Singh, W.F.D. Bennett, C. Arnarez, T.A. Wassenaar, L.V. Schäfer, X. Periole, D.P. Tieleman, S.J. Marrink, Improved parameters for the martini coarse-grained protein force field, J. Chem. Theory Comput. 9 (2013) 687–697.
[33] X. Periole, M. Cavalli, S.J. Marrink, M.A. Ceruso, Combining an elastic network with a coarse-grained molecular force field: Structure, dynamics, and intermolecular recognition, J. Chem. Theory Comput. 5 (2009) 2531–2543.
[34] M. Nonnenmacher, W. Wang, M.A. Child, X.Q. Ren, C. Huang, A.Z. Ren, J. Tocci, Q. Chen, K. Bittner, K. Tyson, N. Pande, C.H.Y. Chung, S.M. Paul, J. Hou, Rapid evolution of blood-brain-barrier-penetrating AAV capsids by RNA-driven biopanning, Mol. Ther. 20 (2021) 366–378.
[35] J. Piedra, M. Ontiveros, S. Miravet, C. Penalva, M. Monfar, M. Chillon, Development of a rapid, robust, and universal PicoGreen-based method to titer adeno-associated vectors, Hum. Gene Ther. Methods 26 (2015) 35–42.
[36] A.M. Davidoff, C.Y.C. Ng, J. Zhou, Y. Spence, A.C. Nathwani, Sex significantly influences transduction of murine liver by recombinant adeno-associated viral vectors through an androgen-dependent pathway, Blood 102 (2003) 480–488.
[37] Y. Peng, H. Jin, Y.H. Xue, Q. Chen, S.Y. Yao, M.Q. Du, S. Liu, Current and future therapeutic strategies for Alzheimer's disease: an overview of drug development bottlenecks, Front. Aging Neurosci. 3 (15) (2023) 1206572.
[38] C.K. Kim, Y.R. Lee, L. Ong, M. Gold, A. Kalali, J. Sarkar, Alzheimer's disease: key insights from two decades of clinical trial failures, J. Alzheimer's Dis. 87 (2022) 83–100.
[39] J. Cummings, Y. Zhou, G. Lee, K. Zhong, J. Fonseca, F. Cheng, Alzheimer's disease drug development pipeline: 2023, Alzheimer's Dement. 9 (2) (2023) 12385.
[40] C.J. Swanson, Y. Zhang, S. Dhadda, J. Wang, J. Kaplow, R.Y.K. Lai, L. Lannfelt, H. Bradley, M. Rabe, A. Koyama, L. Reyderman, D.A. Berry, S. Berry, R. Gordon, L. D. Kramer, J.L. Cummings, A randomized, double-blind, phase 2b proof-of-concept clinical trial in early Alzheimer's disease with lecanemab, an anti-Aβ protofibril antibody, Alzheimers Res. Ther. 13 (1) (2021) 80.
[41] J. Sevigny, P. Chiao, T. Bussière, P.H. Weinreb, L. Williams, M. Maier, R. Dunstan, S. Salloway, T. Chen, Y. Ling, J. O'Gorman, F. Qian, M. Arastu, M. Li, S. Chollate, M.S. Brennan, O. Quintero-Monzon, R.H. Scannevin, H.M. Arnold, T. Engber, K. Rhodes, J. Ferrero, Y. Hang, A. Mikulskis, J. Grimm, C. Hock, R.M. Nitsch, A. Sandrock, The antibody aducanumab reduces Aβ plaques in Alzheimer's disease, Nature 537 (2016) 50–56.
[42] W.K. Self, D.M. Holtzman, Emerging diagnostics and therapeutics for Alzheimer disease, Nat. Med 29 (2023) 2187–2199.
[43] A.L. Boxer, R. Sperling, Accelerating Alzheimer's therapeutic development: the past and future of clinical trials, Cell 186 (2023) 4757–4772.
[44] S. Gupta, A.J. Moreno, D. Wang, J. Leon, C. Chen, O. Hahn, Y. Poon, K. Greenberg, N. David, T. Wyss-Coray, D. Raftery, D.E.L. Promislow, D.B. Dubal, KL1 domain of longevity factor klotho mimics the metabolome of cognitive stimulation and enhances cognition in young and aging mice, J. Neurosci. 42 (2022) 4016–4025.
[45] R. Dash, H.J. Choi, I.S. Moon, Mechanistic insights into the deleterious roles of Nasu-Hakola disease associated TREM2 variants, Sci. Rep. 10 (1) (2020) 3663.
[46] L. Chen, L. Fu, J. Sun, Z. Huang, M. Fang, A. Zinkle, X. Liu, J. Lu, Z. Pan, Y. Wang, G. Liang, X. Li, G. Chen, M. Mohammadi, Structural basis for FGF hormone signalling, Nature 618 (2023) 862–870.
[47] G. Chen, Y. Liu, R. Goetz, L. Fu, S. Jayaraman, M.C. Hu, O.W. Moe, G. Liang, X. Li, M. Mohammadi, α-Klotho is a non-enzymatic molecular scaffold for FGF23 hormone signalling, Nature 553 (2018) 461–466.
[48] M. Fakhar, Najumuddin, S. Zahid, S. Rashid, Structural basis of Klotho binding to VEGFR2 and TRPC1 and repurposing calcium channel blockers as TRPC1 antagonists for the treatment of age-related cardiac hypertrophy, Arch. Biochem. Biophys. 15 (719) (2022) 109171.
[49] A. Tuuttila, E. Morgunova, U. Bergmann, Y. Lindqvist, K. Maskos, C. Fernandez-Catalan, W. Bode, K. Tryggvason, G. Schneider, Three-dimensional structure of human tissue inhibitor of metalloproteinases-2 at 2.1 A resolution, J. Mol. Biol. 284 (1998) 1133–1140.
[50] J. Batra, A.S. Soares, C. Mehner, E.S. Radisky, Matrix Metalloproteinase-10/TIMP-2 structure and analyses define conserved core interactions and diverse exosite interactions in MMP/TIMP Complexes, PLoS One 8 (9) (2013) e75836.
[51] E. Morgunova, A. Tuuttila, U. Bergmann, K. Tryggvason, R. Huber, Structural insight into the complex formation of latent matrix metalloproteinase 2 with tissue inhibitor of metalloproteinase 2, Proc. Natl. Acad. Sci. USA 99 (2002) 7414–7419.
[52] S.M. Kim, B.R. Mun, S.J. Lee, Y. Joh, H.Y. Lee, K.Y. Ji, H.R. Choi, E.H. Lee, E. M. Kim, J.H. Jang, H.W. Song, I. Mook-Jung, W.S. Choi, H.S. Kang, TREM2 promotes Aβ phagocytosis by upregulating C/EBPα-dependent CD36 expression in microglia, Sci. Rep. 7 (1) (2017) 11118.

[53] L. Zhong, X.F. Chen, T. Wang, Z. Wang, C. Liao, Z. Wang, R. Huang, D. Wang, X. Li, L. Wu, L. Jia, H. Zheng, M. Painter, Y. Atagi, C.C. Liu, Y.W. Zhang, J.D. Fryer, H. Xu, G. Bu, Soluble TREM2 induces inflammatory responses and enhances microglial survival, J. Exp. Med. 214 (2017) 597–607.
[54] X. Sheng, Y. Yao, R. Huang, Y. Xu, Y. Zhu, L. Chen, L. Zhang, W. Wang, R. Zhuo, D. Can, C.F. Chang, Y. wu Zhang, H. Xu, G. Bu, L. Zhong, X.F. Chen, Identification of the minimal active soluble TREM2 sequence for modulating microglial phenotypes and amyloid pathology, J. Neuroinflamm. 18 (1) (2021) 286.
[55] F. Filipello, C. Goldsbury, S.F. You, A. Locca, C.M. Karch, L. Piccio, Soluble TREM2: innocent bystander or active player in neurological diseases? Neurobiol. Dis. 165 (2022) 105630.
[56] B.R. Price, T.L. Sudduth, E.M. Weekman, S. Johnson, D. Hawthorne, A. Woolums, D.M. Wilcock, Therapeutic Trem2 activation ameliorates amyloid-beta deposition and improves cognition in the 5XFAD model of amyloid deposition, J. Neuroinflamm. 17 (1) (2020) 238.
[57] A.C. Ferreira, B.M. Hemmer, S.M. Philippi, H. Liu, J.D. Zhu, T. Kareva, T. Ahfeldt, M. Varghese, P.R. Hof, J.M. Castellano, MAL Neuronal TIMP2 regulates hippocampus-dependent plasticity and extracellular matrix complexity, Mol. Psychiatry 28 (2023) 3943–3954.
[58] M. Fassler, C. Benaim, J. George, TREM2 agonism with a monoclonal antibody attenuates tau pathology and neurodegeneration, Cells 12 (11) (2023) 1549.
[59] C.Y. Zeng, T.T. Yang, H.J. Zhou, Y. Zhao, X. Kuang, W. Duan, J.R. Du, Lentiviral vector–mediated overexpression of Klotho in the brain improves Alzheimer's disease–like pathology and cognitive deficits in mice, Neurobiol. Aging 78 (2019) 18–28.
[60] N. Zhao, W. Qiao, F. Li, Y. Ren, J. Zheng, Y.A. Martens, X. Wang, L. Li, C.C. Liu, K. Chen, Y. Zhu, T.C. Ikezu, Z. Li, A.D. Meneses, Y. Jin, J.A. Knight, Y. Chen, L. Bastea, C. Linares, B. Sonustun, L. Job, M.L. Smith, M. Xie, Y.U. Liu, A. D. Umpierre, K. Haruwaka, Z.S. Quicksall, P. Storz, Y.W. Asmann, L.J. Wu, G. Bu, Elevating microglia TREM2 reduces amyloid seeding and suppresses disease-associated microglia, J. Exp. Med. 219 (12) (2022) e20212479.
[61] A. Vilalta, Y. Zhou, J. Sevalle, J.K. Griffin, K. Satoh, D.H. Allendorf, S. De, M. Puigdellívol, A. Bruzas, M.A. Burguillos, R.B. Dodd, F. Chen, Y. Zhang, P. Flagmeier, L.M. Needham, M. Enomoto, S. Qamar, J. Henderson, J. Walter, P. E. Fraser, D. Klenerman, S.F. Lee, P.S. George-Hyslop, G.C. Brown, Wild-type sTREM2 blocks Aβ aggregation and neurotoxicity, but the Alzheimer's R47H mutant increases Aβ aggregation, J. Biol. Chem. 296 (2021) 100631.
[62] W. Qiao, Y. Chen, J. Zhong, B.J. Madden, C.M. Charlesworth, Y.A. Martens, C. C. Liu, J. Knight, T.C. Ikezu, K. Aishe, Y. Zhu, A. Meneses, C.L. Rosenberg, L. A. Kuchenbecker, L.K. Vanmaele, F. Li, K. Chen, F. Shue, M.V. Dacquel, J. Fryer, A. Pandey, N. Zhao, G. Bu, Trem2 H157Y increases soluble TREM2 production and reduces amyloid pathology, Mol. Neurodegener. 18 (1) (2023) 8.